The co-phasing detection method for sparse optical synthetic aperture systems*

Liu Zheng(刘 政)[a)b)†], Wang Sheng-Qian(王胜千)[a)], and Rao Chang-Hui(饶长辉)[a)]

[a)] *Key Laboratory on Adaptive Optics, Institute of Optics and Electronics, Chinese Academy of Sciences, Chengdu* 610209, *China*

[b)] *College of Photon–Electron Science and Engineering, National University of Defense Technology, Changsha* 410073, *China*

(Received 9 February 2012; revised manuscript received 5 March 2012)

Co-phasing between different sub-apertures is important for sparse optical synthetic aperture telescope systems to achieve high-resolution imaging. For co-phasing detection in such a system, a new aspect of the system's far-field interferometry is analysed and used to construct a novel method to detect piston errors. An optical setup is built to demonstrate the efficacy of this method. Experimental results show that the relative differences between measurements by this method and the criterion are less than 4%, and their residual detecting errors are about 0.01 λ for different piston errors, which makes the use of co-phasing detection within such a system promising.

Keywords: sparse-optical-synthetic-aperture, co-phasing detection, piston error

PACS: 95.55.Cs, 42.30.Va, 42.15.Fr **DOI:** 10.1088/1674-1056/21/6/069501

1. Introduction

In a sparse optical synthetic aperture (SOSA) system, the piston error, which means the entire offset between wave fronts of different sub-apertures (different from the "piston" depicting the discontinuous optical surface between adjacent segment mirrors), must be detected and corrected to achieve high-resolution imaging.[1−6] For such systems, different methods have been proposed to improve this co-phasing detection technique. For example, the fringe tracking (FPT) algorithm is used to decouple piston errors using the relationships between some features of the interference fringes and piston errors.[7,8] The phase diversity (PD) algorithm, based on the probabilistic information theory, could recover wave fronts from in-focus and out-of-focus images.[9−11] For the detection using special devices, such as pyramid mirrors, the piston error needs to be calculated based on some of the special optical properties of these devices.[12−14]

Furthermore, another way to detect piston errors is to use the far-field interferometric information of the system, and some experts have been interested in this area.[15−17] Horrobin *et al.*[16] fitted the envelope of the far-field intensity (FFI) of a system using the Gauss function to calculate the piston errors from the envelope-removed fringes. Ni *et al.*[17] proposed a method of combining the variations in the side lobe intensity of the module transfer function (MTF) and the symmetry of the point spread function (PSF) with the aid of a PD algorithm to analyse and detect the piston errors of the Star-9 system.

On the other hand, methods of detecting the discontinuous surface between adjacent segment-mirrors in segmented primary mirror systems also provide a valuable reference for our focus, although they are concerned with different kinds of systems. For example, Chanan *et al.*[18,19] made use of the information about side-lopes to calculate the discontinuous surface between adjacent segment-mirrors in the Keck telescope. And Zhao and Cao[20] analysed an algorithm based on an interferometric pattern and testified its usage in detecting the discontinuous optical surface between adjacent mirror experiments, in which a residual detecting error of 0.03 λ was obtained.[20] Aiming at detecting the discontinuous optical surface between adjacent segments, these methods probably need to be further verified before confirming their effectiveness for the co-phasing detection of the SOSA system.

In this paper, we study a new method to detect the piston error, which takes a point of view that is different from that mentioned above. A new aspect regarding the system's far-field information—the sim-

*Project supported by the Young Scientists Fund of the National Natural Science Foundation of China (Grant No. 61008038).

†Corresponding author. E-mail: liuzhengIOE@yeah.net

© 2012 Chinese Physical Society and IOP Publishing Ltd

ilarity embodied between the far-field intensities of the system and the referenced sub-aperture—is analysed and utilized to compose the piston decoupling algorithm for the first time. From its theoretical basis, it is seen that this method is new and different compared with some of the methods using far-field interferometry, such as the side-lopes information studied by Chanan *et al.*,[18,19] the interferometric pattern studied by Zhao and Cao,[20] and also the one studied by Ni *et al.*.[17] Furthermore, we build an optical setup to demonstrate the ability of this new method by using a sensitive micro-displacement sensor (SMDS) as the criterion. Experimental results show that the relative differences between the measurements of this method and the criterion are less than 4%, and the residual detecting errors are about 0.01 λ for different piston errors, which means that it may be used to perform co-phasing detection with enough accuracy and a valuable reference for relevant concerns.

2. Theory

The structure of the optical pupil of the SOSA system is shown in Fig. 1, where each sub-aperture has a diameter of $2a$, with a centre coordinate of n-th, sub-aperture at (ε_n, η_n), and corresponding polar coordinate (ρ_n, θ_n).

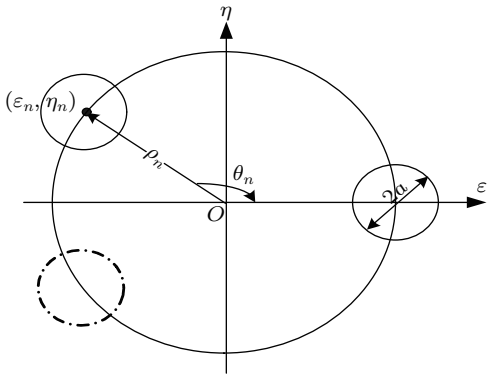


Fig. 1. The optical pupil of the SOSA system.

The system complex pupil function is expressed as[21]

$$P(\varepsilon,\eta)=\sum_{n=1}^{N}\{\Pi(\varepsilon,\eta)\exp[\,\mathrm{j}kw_n(\varepsilon,\eta)]\}*\delta(\varepsilon_n,\eta_n), \tag{1}$$

where (ε,η) is the coordinate of the pupil plane, "$*$" represents the convolution operation, wave number $k=2\pi/\lambda$, "N" is the total number of sub-apertures, $w_n(\varepsilon,\eta)$ is the Zernike aberration of the n-th sub-aperture, and $\Pi(\varepsilon,\eta)$ is the sub-aperture pupil function, and is expressed as[22]

$$\Pi(\varepsilon,\eta)=\mathrm{circ}\Big(\frac{\sqrt{\varepsilon^2+\eta^2}}{a}\Big). \tag{2}$$

The impulse function $\delta(\varepsilon_n,\eta_n)$ in Eq. (1) represents the centre of the n-th sub-aperture, and is expressed as

$$\delta(\varepsilon_n,\eta_n)=\delta(\varepsilon-\rho_n\cos\theta_n,\eta-\rho_n\sin\theta_n). \tag{3}$$

According to the principle of Fourier optics,[23] the transfer function of the system complex amplitude is

$$\begin{aligned}&A(u,v)\\&=\Im\{P(\varepsilon,\eta)\}\\&=\Im\Big\{\sum_{n=1}^{N}\{\Pi(\varepsilon,\eta)\exp[\,\mathrm{j}kw_n(\varepsilon,\eta)]\}*\delta(\varepsilon_n,\eta_n)\Big\}\\&=\sum_{n=1}^{N}\Big[\Im\{\exp[\,\mathrm{j}k\cdot f_n(\varepsilon,\eta)]\}*\frac{a\mathrm{J}_1(2\pi a\sqrt{u^2+v^2})}{\sqrt{u^2+v^2}}\Big]\\&\quad\times\exp[\,\mathrm{j}k(\alpha_n-\lambda u\varepsilon_n-\lambda v\eta_n)],\end{aligned} \tag{4}$$

where (u,v) is the coordinate concerning spatial frequency, J_1 means the first-order Bessel function, $\Im[\cdot]$ indicates the two-dimensional Fourier transformer, and α_n and $f_n(\varepsilon,\eta)$, respectively, denote the mean value and the zero-mean-normalized part of the n-th sub-aperture Zernike aberration.

If the aberrations within each sub-aperture are corrected using adaptive optics, or for the applications of the SOSA system within the space where the aberrations caused by the atmosphere can be ignored, $f_n(\varepsilon,\eta)$ can be assumed to be zero. Then equation (4) is approximated by

$$\begin{aligned}A(u,v)=&\sum_{n=1}^{N}\frac{a\mathrm{J}_1(2\pi a\sqrt{u^2+v^2})}{\sqrt{u^2+v^2}}\\&\times\exp[\,\mathrm{j}k(\alpha_n-\lambda u\varepsilon_n-\lambda v\eta_n)].\end{aligned} \tag{5}$$

Then the point spread function (PSF) in the spatial frequency domain is described as

$$\begin{aligned}&I(u,v)\\&=|A(u,v)|^2\\&=\Big|\sum_{n=1}^{N}\frac{a\mathrm{J}_1(2\pi a\sqrt{u^2+v^2})}{\sqrt{u^2+v^2}}\\&\quad\times\exp[\,\mathrm{j}k(\alpha_n-\lambda u\varepsilon_n-\lambda v\eta_n)]\Big|^2\\&=\frac{a^2\mathrm{J}_1^2(2\pi a\sqrt{u^2+v^2})}{u^2+v^2}\\&\quad\times\Big|\sum_{n=1}^{N}\exp[\,\mathrm{j}k(\alpha_n-\lambda u\varepsilon_n-\lambda v\eta_n)]\Big|^2.\end{aligned} \tag{6}$$

As piston errors exist only among different sub-apertures, we can take one sub-aperture as the refer-

ence one and mark it as aperture 0, and mark other sub-apertures as sub-aperture $1, 2, \ldots, N-1$ (adjusting the corresponding subscripts), then equation (6) is expressed as

$$I(u,v) = \frac{a^2 \mathrm{J}_1^2(2\pi a\sqrt{u^2+v^2})}{u^2+v^2} \times \Big|1 + \sum_{n=1}^{N-1} \exp[\,\mathrm{j}k(p_n - \lambda u\varepsilon_{n0} - \lambda v\eta_{n0})]\Big|^2, \tag{7}$$

where $p_n = \alpha_n - \alpha_0$ is the entire offset between different sub-aperture wave-fronts, which represents the piston error between sub-aperture "n" and the reference aperture, and $(\varepsilon_{n0}, \eta_{n0}) = (\varepsilon_n - \varepsilon_0, \eta_n - \eta_0)$ is the deviation of the centre coordinate between sub-aperture "n" and the reference aperture. For bi-aperture systems (or sub-systems with two sub-apertures) whose baseline direction corresponds to the x axis of the image plane, the FFI under the monochromatic target wave (MTW) can be described as follows:

$$I(x,y) = \frac{2a^2\lambda^2 \mathrm{J}_1^2\Big[\dfrac{ka(x^2+y^2)^{1/2}}{f}\Big]}{(x^2+y^2)/f^2} \times \Big[1 + \cos k\Big(\frac{2R}{f}x - p_1\Big)\Big] \tag{8}$$

as described above, where p_1 is the piston error between these two sub-apertures (the reference aperture "0" and the unreferenced aperture "1"), (x, y) is the coordinate on the image plane, "$2R$" denotes the centre distance between them ($(\varepsilon_{10}, \eta_{10}) = (2R, 0)$), and f is the focal length of the imaging device. Under the same conditions, the FFI of the reference sub-aperture is described as

$$I_{\mathrm{si}}(x,y) = \frac{a^2\lambda^2 f^2}{x^2+y^2}\mathrm{J}_1^2\Big(\frac{ka\sqrt{x^2+y^2}}{f}\Big). \tag{9}$$

From Eqs. (8) and (9), it is seen that the theoretical difference in FFI between the whole system and the reference sub-aperture is due mainly to a cosine item directly correlated with the piston error between these two sub-apertures. In light of this point, we define a function D_p which describes the similarities of the FFI between the whole system and the reference sub-aperture under unique imaging conditions. A mathematical description of D_p is[24]

$$D_p(x,y) = \frac{I(x,y)/2 - I_{\mathrm{si}}(x,y)}{I_{\mathrm{si}}(x,y)}, \tag{10}$$

where I and I_{si} represent the system FFI and the reference sub-aperture FFI, respectively. After some derivations using Eqs. (8)–(10), the theoretical result of D_p is expressed as follows:

$$D_p(x,y) = \cos k\Big(\frac{2R}{f}x - p_1\Big). \tag{11}$$

From this equation, it is seen that D_p is determined mainly by the piston error, with the corresponding effect to the distribution of D_p only along the x axis (corresponding to the baseline direction of the two sub-apertures). Then the piston error "p_1" can be solved when D_p reaches a maximum along the x axis, as follows:

$$p_1 = \frac{2R}{f}x_{\mathrm{c}} + h\lambda,\ h \in Z, \tag{12}$$

where x_{c} is the value of the x coordinate where D_p reaches a maximum, and λ is the wavelength. From this equation, we can see that the piston error is solved theoretically from x_{c}, which includes the "$h\lambda$" item. Theoretically, if the variation in piston error is no more than one wavelength, or for the case of piston error no more than λ, we can calculate it by comparing the values to the right of "=" in Eq. (12) before and after the piston error changes, and the result is as follows:

$$\Delta p_1 = \frac{2R}{f} \cdot (x_{\mathrm{c}2} - x_{\mathrm{c}1}), \tag{13}$$

where Δp_1 means the piston variation, and $x_{\mathrm{c}1}$ and $x_{\mathrm{c}2}$ represent the values of X_{c} before and after the piston error changes, respectively. Based on Eq. (13), a piston error (or its variations) no more than λ can be directly detected by analysing the distribution of D_p before and after the piston error changes, while there is no need for iterations or matrix calculations in this detection procedure.

In addition, to guarantee the detection accuracy at the sub-pixel level, x_{c} is modified in the experiment using the following quadric-curve interpolation:[25,26]

$$x_{\mathrm{c}} = d_{\mathrm{pixel}}\Big[x_m + \frac{1}{2}\frac{D_p(x_m-1) - D_p(x_m+1)}{D_p(x_m-1) + D_p(x_m+1) - 2\cdot D_p(x_m)}\Big], \tag{14}$$

where x_m is the integer value of x_{c}, $D_p\ (x_m - 1)$ and $D_p(x_m + 1)$ represent the values of D_p at the pixels to the left and right of x_m along the x axis, respectively. d_{pixel} denotes the width of the camera pixel.

Using Eq. (14), equation (12) can be specified to describe the real-time detection result for a certain state (before or after the piston error changes):

$$p_1 = \frac{2R}{f} \cdot d_{\mathrm{pixel}}\Big[x_m + \frac{1}{2} \cdot \frac{D_p(x_m-1) - D_p(x_m+1)}{D_p(x_m-1) + D_p(x_m+1) - 2\cdot D_p(x_m)}\Big] + h\lambda. \tag{15}$$

And the piston error or its variation no more than λ is calculated using Eqs. (13) and (15) as

$$\Delta p_1 = \frac{2R \cdot d_{\text{pixel}}}{f} \cdot \left\{ \left[x_m + \frac{1}{2} \cdot \frac{D_p(x_m - 1) - D_p(x_m + 1)}{D_p(x_m - 1) + D_p(x_m + 1) - 2 \cdot D_p(x_m)} \right]_2 - \left[x_m + \frac{1}{2} \cdot \frac{D_p(x_m - 1) - D_p(x_m + 1)}{D_p(x_m - 1) + D_p(x_m + 1) - 2 \cdot D_p(x_m)} \right]_1 \right\}, \tag{16}$$

where subscripts "1" and "2" denote the states before and after the piston error changes, respectively (subscripts "1" and "2" are applied to neither D_p nor x_m because the distributions of function D_p before and after the piston error changes are probably different).

In this section, we have studied the FFI of the SOSA system from the basic theory of Fourier optics. Beyond this, the similarity embodied between the far-field intensity of the system and the referenced sub-aperture, and its relationship to the piston error, have also been analysed and utilized in the piston decoupling algorithm.

As shown above, this method uses a new aspect of far-field interferometry to solve the piston error, and is different from the common methods.[17–20] In the following section, we will use a deformable mirror (DM) with separated circular sub-mirrors to introduce piston errors between two sub-apertures and construct an active co-phasing detection test-bed (ACDT) to testify the efficacy of this method.

3. Experiment

3.1. Description of the test-bed

A block diagram of the ACDT setup presented in this paper is shown in Fig. 2. The ACDT is a modular system that consists of various modules such as source (SM), beam splitting (BSM), piston error introduction (PEIM), piston error calibration (PECM), and piston error detection (PEDM) modules, and a computer control system (CCS). The optical layout of the ACDT is shown in Fig. 3.

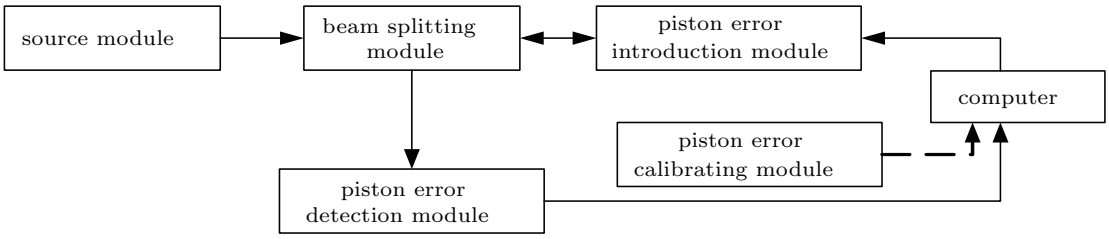


Fig. 2. A block diagram of the ACDT.

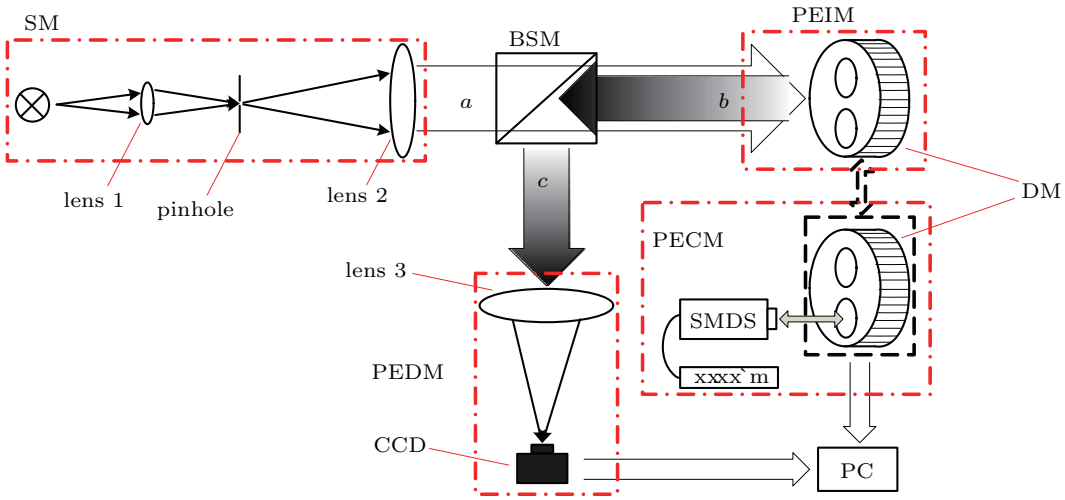


Fig. 3. (colour online) The optical layout of the ACDT.

A semiconductor laser with a wavelength of 632 nm is used as a light source for the experiment. After passing through the lens and the pinhole, the collimated plane output illuminates the BSM. After the BSM, the plane wave (beam "*a*") reaches the DM of the PEIM. The DM contains two sub-mirrors placed at a certain distance, with the back of each mirror supported by three piezoelectric transducer (PZT) actuators. A wave-absorbing material covers the other areas, aside from the two sub-mirrors on the surface of the DM. Thus, when the voltages imposed on the three actuators of a sub-mirror, which is later referred to as the unreferenced sub-mirror, are changed by the same amount, the beam reflected by the sub-mirrors (beam "*b*") can simulate the output of a SOSA system containing the piston error between the two aberration-free sub-apertures. Moreover, the introduced piston error is closely related to the displacement of the unreferenced sub-mirror.

After being reflected by BSM, the output of PEIM (beam "*b*") turns into the PEDM. The FFI images are recorded by a CCD camera placed in the focal plane of lens 3 ($f = 1000$ mm). The pixel width is 8.30 μm, and the resolution is 782 pixels × 582 pixels. After shielding the unreferenced sub-mirror, the diameter of the Airy disk of the other sub-mirror (the referenced one) covers about 23 pixels on the camera. Using the images captured by the CCD, the variations in piston error can be calculated based on the theory presented in Section 2.

The PECM is designed to evaluate the proposed method by calibrating the piston errors first. In the PECM, the displacements of the unreferenced sub-mirror are tested using a sensitive micro-displacement sensor (SMDS, Fig. 5) for the same voltages used in introducing the piston error in the PEIM. Based on the optical path of the ACDT, the detected piston error should be twice as large as the displacement of the unreferenced sub-mirror, i.e.,

$$\Delta p_1 = 2\Delta p_m, \tag{17}$$

where Δp_1 is the piston error detected by using the proposed method, and Δp_m is the displacement calibrated by SMDS when the voltages imposed on the actuators of the unreferenced sub-mirror are increased by Δv. Thus, this method can be validated by investigating the coherence between Δp_1 and $2\Delta p_m$ in the experiment.

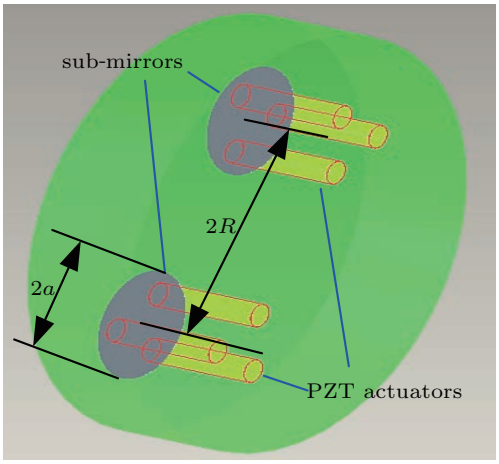


Fig. 4. (colour online) The structure and parameters of DM, where $R = 7$ mm and $a = 4$ mm.

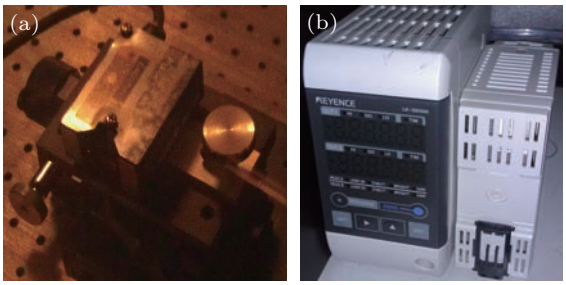


Fig. 5. (colour online) An image of the SMDS: (a) the sensor head, (b) the display screen and power supply.

3.2. Experiment

The experiment is composed of three processes, namely, setup, calibration, and detection (Fig. 6). Herein, the voltage state means a state where a certain voltage is imposed on the three actuators of the unreferenced sub-mirror.

In the setup process, the optical collimations between the different sub-systems in the ACDT should be first confirmed. Then, the unreferenced sub-mirror is shielded to obtain the images of the FFI of the reference sub-aperture [$I_{\rm si}$ in Eq. (10)].

The aim of the calibration process is to detect the values of Δp_m that will be used for the validation of this proposed method afterwards. The SMDS is directly used to record a set of different voltages (Δv), with their corresponding values of Δp_m no more than 0.5λ, which makes the introduced piston error no more than λ, according to Eq. (17). In a specific operation, numerous measurements are averaged to make the results more accurate than the displayed accuracy of SMDS.[27]

More than 100 images are captured continuously for a certain voltage state in the detection process (V_0

or $V_0 + \Delta v$). The FFI of the system [I in Eq. (10)] is used along with I_{si} to obtain the real-time measurement corresponding to each image. The average of the results from these images is considered as the actual piston error of the corresponding voltage state [p_1 in Eq. (15)]. Thus, the variations in piston error [Δp_1 in Eq. (16)] can be obtained by subtracting the "p_1" of the V_0 state from the one of the $V_0+\Delta v$ state. Finally, the results of Δp_1 and $2\Delta p_m$, along with their relative differences and absolute differences, which represent the residual detecting errors, are presented to demonstrate the efficacy of this method.

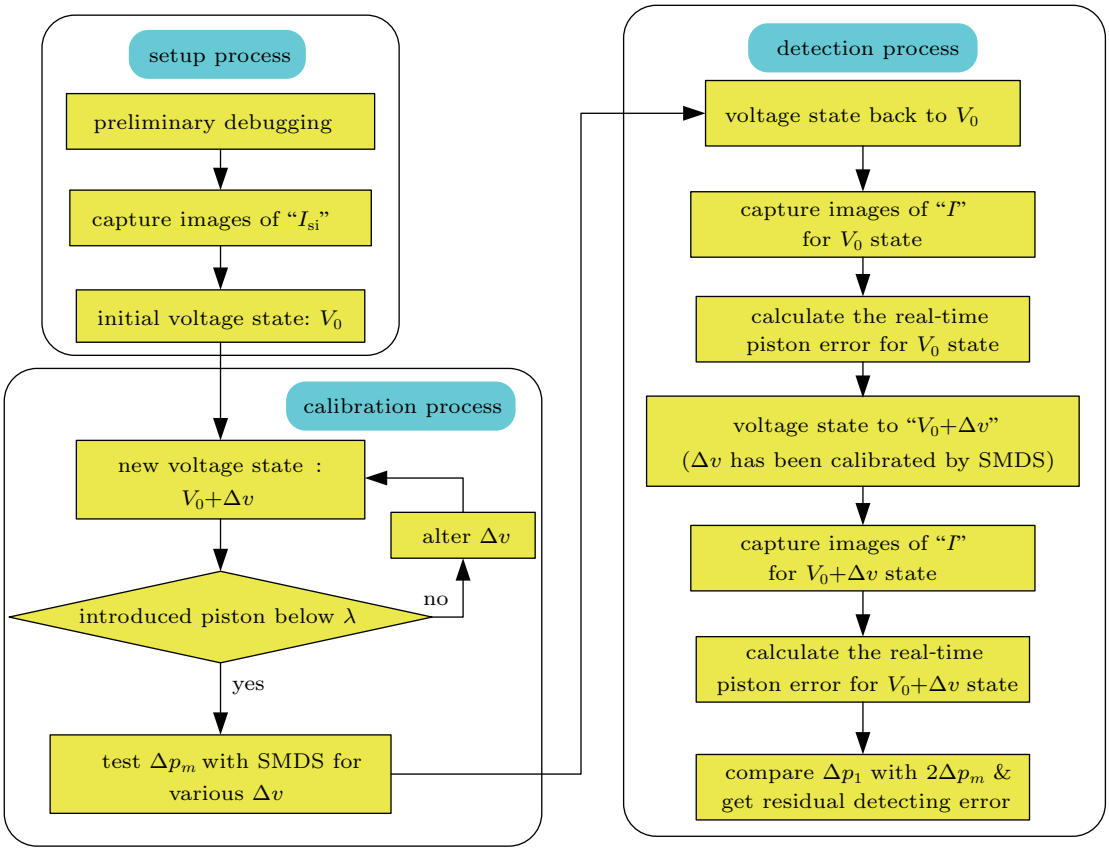


Fig. 6. (colour online) Flowchart of the experiment.

3.3. Results and discussion

The ACDT is installed on a vibration-isolated air base (Fig. 7).

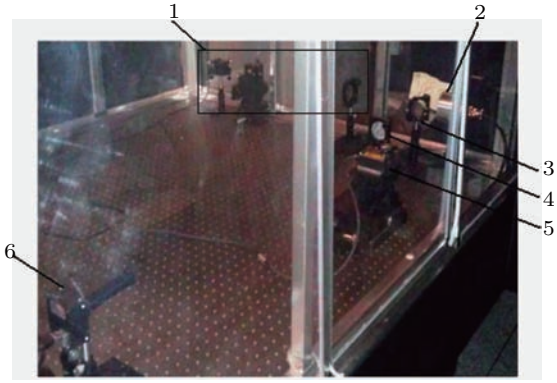


Fig. 7. (colour online) An image of the ACDT: 1 SM, 2 DM, 3 BSM, 4 lens 3, 5 SMDS, and 6 CCD.

According to the flowchart in Fig. 6, the experiment is conducted on the ACDT. In the calibration process, several different values of "Δv" are recorded, while their corresponding results of Δp_m are less than 0.5λ. Then they are used in the detection process to compare the results of Δp_1 and $2\Delta p_m$ based on the flowchart of Fig. 6. A group of photos of the FFI system for different voltage states are shown in Fig. 8.

According to the principle presented in Section 2 and the flowchart of Fig. 6, the piston error is solved using the D_p function based on the recorded FFIs of the system and the reference sub-aperture. To lower the influence of the noise, average backgrounds are subtracted from each recorded image. The results of Δp_1 and $2\Delta p_m$ are shown in Fig. 9, with the relative differences indicated in Fig. 10, from which the residual detecting errors can be calculated.

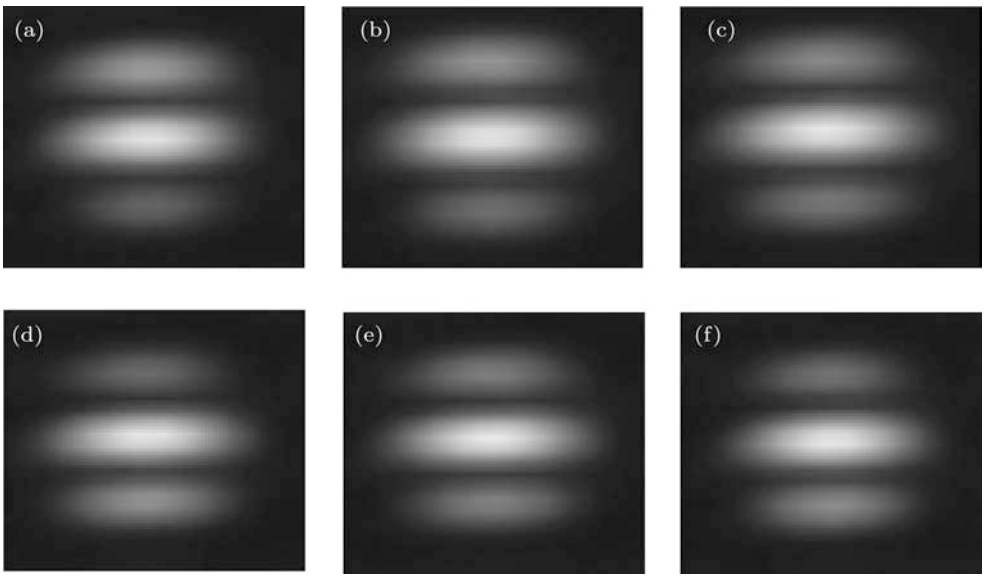


Fig. 8. Photos of the FFI system for voltage states of (a) "$V_0 + \Delta v_1$", (b) "$V_0 + \Delta v_2$", (c) "$V_0 + \Delta v_3$", (d) "$V_0 + \Delta v_4$", (e) "$V_0 + \Delta v_5$", (f) "$V_0 + \Delta v_6$".

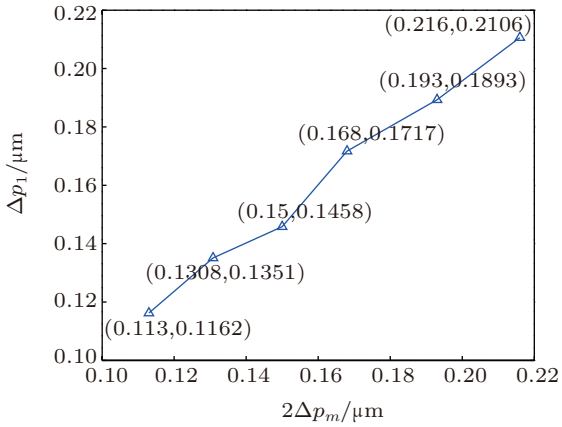


Fig. 9. (colour online) The results of Δp_1 and $2\Delta p_m$.

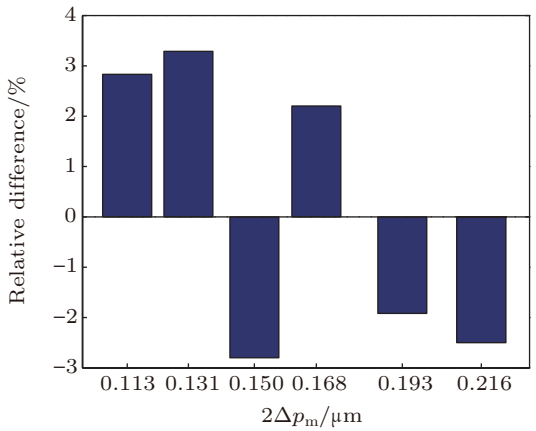


Fig. 10. (colour online) The relative differences between Δp_1 and $2\Delta p_m$.

In Fig. 9, we can see that with the voltage state varying from "$V_0 + \Delta v_1$" to "$V_0 + \Delta v_6$", the corresponding piston error (introduced and calibrated by SMDS) increases gradually, which is in accordance with the change in far-field distribution shown in Fig. 8.

Most importantly, it is shown that the measurements using this method are generally consistent with the results of SMDS. The relative difference between the detection results (Δp_1) and the references ($2\Delta p_m$) are all below 4%, and sometimes even less than 2%. Moreover, the residual detecting errors calculated from these results show that for different piston errors, the residual detection errors of this method are within 0.01λ (about 0.0063 μm).

Meanwhile, it can be seen that the consistencies between Δp_1 and $2\Delta p_m$ change for different values of Δv (Fig. 10). This phenomenon is probably attributed to two factors. The first comes from the hysteretic response of the PZT actuators of the DM, where a number of images need to be captured and recorded in the detection process. Thus, the time it spends in the detection process for a certain voltage state is slightly longer than that needed in the Δp_m testing procedure. Therefore, the detection process is more vulnerable to the hysteric response of the PZT actuators, indicating that for different values of Δv, the influences of different levels of such a response are more evident in the results of Δp_1. The other factor comes from the effects of different kinds of noise. After subtracting the background for each image captured during the detection procedure, the experiment still confronts different kinds of noise such as the dark-current and the photon noises from the CCD. Therefore, different levels of noise for different values of Δv may contribute to

this phenomenon. But from the final results we can see that this phenomenon does not evidently influence the detection accuracy.

According to the above analyses, it is obvious that this new method has some different characteristics compared with the other methods, as listed below.

Firstly, unlike the other methods, this co-phasing detection method takes a different point of view to detecting the piston error. In its algorithm, the similarity embodied between the far-field intensities of the system and the referenced sub-aperture is utilized to solve the piston error, which is new and different from the common methods.[17−20] To the best of our knowledge, this algorithm has not been proposed elsewhere.

Secondly, the experimental results show that the detection accuracy of this new method is slightly better than that of some of the recent results obtained by other researchers,[17−20] although some of these are for a different kind of system. This is important because it indicates that this method is capable of conducting co-phasing detection with a high-enough accuracy.

4. Conclusion

A new way to detect the piston error is introduced, and the theory of this method is explained in this paper. An optical system is built in the laboratory to analyse the characteristics of this method, and the corresponding results demonstrate its feasibility. This method is different from other far-field interferometry methods in that it is based on a new aspect of the far-field features of the SOSA system, and is also able to achieve high-enough accuracy. It is likely to be a promising choice for relevant applications of sparse optical synthetic aperture systems.

References

[1] Meinel A B 1970 *Appl. Opt.* **9** 2501

[2] Burton D O and De Hainaut C R 1990 *Proc. SPIE* **1236** 406

[3] Loreggia D, Gardiol D and Gai M 2004 *Appl. Opt.* **43** 721

[4] Nicholas J M, Matthew P D and Bradley D D 2007 *Appl. Opt.* **46** 5933

[5] Yue J Y, Liu H, Lu Z W, Xu W B, Zhang H, Zhang H X and Liu Y 2010 *Chin. Phys.* B **19** 010702

[6] Liu Z, Wang S Q, Huang L H and Rao C H 2011 *Acta Phys. Sin.* **60** 100702 (in Chinese)

[7] Dame L 1993 *Proc. SPIE* **1947** 161

[8] Robert K and Tyson W 1991 *Proc. SPIE* **1542** 62

[9] Paxman R G and Fienup J R 1988 *J. Opt. Soc. Am.* A **5** 914

[10] Bolcar M R and Fienup J R 2009 *Appl. Opt.* **48** A5

[11] Li F and Rao C H 2011 *High Power Laser and Particle Beams* **3** 37 (in Chinese)

[12] Robert D S and Alice L P 2001 *Proc. SPIE* **4441** 60

[13] Diolaiti, Tozzi A, Ragazzoni R and Ferruzi D 2003 *Proc. SPIE* **4839** 299

[14] Wang J X, Bai F Z, Ning Y and Jiang W H 2011 *Acta Phys. Sin.* **60** 029501 (in Chinese)

[15] Moser L, Eckart A, Horrobin M, Lindhorst B and Rost S 2010 *Proc. SPIE* **7734** 77342X1

[16] Horrobin M, Eckart A, Lindhorst B, Lindhorst U, Moser L and Rost S 2010 *Proc. SPIE* **7734** 77341X1

[17] Ni M, Benson L, Camp J and Herman B 2010 *Opt. Express* **18** 13051

[18] Chanan G, Ohara C and Troy M 2000 *Appl. Opt.* **39** 4706

[19] Chanan G, Troy M and Ohara C 2000 *Proc. SPIE* **4003** 188

[20] Zhao W R and Cao G R 2011 *Opt. Express* **19** 8670

[21] Watson S M, Mills J P and Rogers S K 1988 *J. Opt. Soc. Am.* A **5** 893

[22] Born M and Wolf E 1975 *Principles of Optics-Electromagnetic Theory of Propagation, Interference and Diffraction of Light* 5th edn. (New York: Pergamon) pp. 517–520

[23] Goodman J R 1968 *Introduction to Fourier Optics* (Columbus: McGraw-Hill Press) pp. 36–40

[24] Liu Z, Wang S Q and Rao C H 2012 *Acta Phys. Sin.* **61** 039501 (in Chinese)

[25] Wang X Y, Yun J J and Zhang Y L 2011 *Chin. Phys.* B **20** 104203

[26] Liu J H and She K 2011 *Acta Phys. Sin.* **60** 124203 (in Chinese)

[27] KEYENCE Corporation 2005 http://www.keyence.com/products/measure/laser/lkg/lkg.php